Simulations of Extreme Ionization and Electron Dynamics in Ultraintense Laser–Cluster Interactions

Andreas Heidenreich, Isidore Last, and Joshua Jortner*
School of Chemistry, Tel Aviv University, Tel Aviv 69978, Israel

Abstract. We present a molecular dynamics (MD) simulation code for the exploration of extreme multielectron ionization and attosecond–femtosecond electron dynamics in elemental and molecular clusters driven by ultraintense (peak intensity $I_M = 10^{15}–10^{16}$ W cm^{-2}), ultrafast (temporal pulse widths $\tau = 10–100$ fs), near infrared (photon frequency 0.35 fs^{-1}) laser fields. Validity conditions are presented for the applicability of classical MD simulations to high-energy electron dynamics, which rest on the localization of the wave packet and the distinguishability of identical particles. We also examine the cluster size domain for the applicability of the MD simulation code where the laser intensity is uniform inside the cluster.

1. INTRODUCTION

Of considerable interest are cluster electron dynamics and nuclear Coulomb explosion (CE) dynamics driven by ultraintense near-infrared laser fields (peak intensities $I_M = 10^{15}–10^{20}$ W cm^{-2}, pulse widths $\tau = 10–100$ fs, photon frequency 0.35 fs^{-1}, and photon energy 1.44 eV).[1–32] Extreme cluster multielectron ionization in ultraintense laser fields is distinct from the electron dynamic response in ordinary fields, where perturbative quantum electrodynamics is applicable, and from the response of a single atomic and molecular species in terms of mechanisms, the ionization level, and the timescales for electron and nuclear dynamics.[1,4,16,21–24,27–31] Extreme multielectron cluster ionization involves three sequential–parallel processes of inner ionization, of nanoplasma formation and response, and of outer ionization,[1,4,21] as introduced by Last and Jortner.[16] Cluster electron dynamics triggers nuclear dynamics, with the outer ionization being accompanied by CE,[1,4,10–20,24–26,31,32] which produced high-energy (1 keV–30 MeV) ions and nuclei in the energy domain of nuclear physics. A realistic endeavor in the context of high-energy ion dynamics pertains to table-top D$^+$+D$^+$ (dd) nuclear fusion driven by CE of deuterium-containing clusters,[11–15,17–20,23,24,28] for which compelling experimental and theoretical evidence was advanced. Predictions[17–20] that CE of deuterium containing heteroclusters (e.g., $(CD_4)_n$, $(D_2O)_n$) will result in considerably higher deuteron energies and dd fusion yields, due to energy-boosting effects, were experimentally confirmed.[13–15] The eighty-year quest for tabletop nuclear fusion driven by chemical reactions was achieved by "cold–hot" dd fusion in the chemical physics laboratory, opening avenues for experimental and technological progress.[20,28] The realm of nuclear reactions driven by cluster CE was extended from dd fusion to nucleosynthesis involving heavy nuclei,[32] which is of interest in the context of nuclear astrophysics.[32,33]

Cluster multielectron ionization, nanoplasma dynamics, and response were explored by theoretical models[1,4,5,7–9,16,21–24,29–32,34,35] and by computer simulations.[1,2,7–9,16,21–30] Microscopic models for the cluster inner ionization level were based on the barrier suppression ionization (BSI) model.[21,27,30] An additional contribution to cluster inner ionization arises from electron impact ionization (EII) induced by high-energy (50 eV–1 MeV) nanoplasma electrons.[1,4,21,27,29,30] Cluster outer ioniza-

*Author to whom correspondence should be addressed.
E-mail: jortner@chemsg1.tau.ac.il

tion, which involves the (partial or complete) sweeping out of the nanoplasma electrons in the laser field, could be modeled by the entire cluster BSI model.[22,29]

Molecular dynamics (MD) simulations allow for the confrontation with the predictions of microscopic or macroscopic models. For a $(A^{q+}(qe))_n$ cluster containing n A^{q+} ions, nq nanoplasma electrons, and N = n(q+1) particles, the computational workload increases as N^2. For extremely charged $(Xe^{q+}(qe))_n$ elemental clusters, which are of interest to us, such MD simulations are practical for q = 3–36 up to n = 3000 (i.e., N = 10^4–10^5). We utilized MD simulations[16,21–24,27–29] for (high-energy) electrons and ions to study inner ionization induced by BSI and EII, nanoplasma formation and response, outer ionization, and ion CE dynamics in elemental and molecular clusters driven by ultraintense (Gaussian or rectangular) laser pulses. Some details of these simulation methods were already reported. In this paper we present a complete description of our MD simulation code, focusing on the methodology and on the validity conditions for the exploration of electron dynamics. This MD simulation code is applicable for extreme ionization, multielectron dynamics, and CE of elemental and molecular clusters. Elemental Xe_n clusters provide a benchmark system for this novel research field.[1,4,21,22] We shall present some representative computational results for the cluster size and laser parameter dependence of extreme multielectron inner/outer ionization in these clusters driven by ultraintense, Gaussian, near-infrared laser fields.

2. MOLECULAR DYNAMICS SIMULATIONS

The laser electric field $F_1(t)$ was taken as

$$F_1(t) = F_{10}(t)\cos(2\pi\nu t) \quad (1)$$

being characterized by a Gaussian-shaped envelope function of the pulse

$$F_{10}(t) = F_M\exp[-4\ln(2)(t/\tau)^2] \quad (2)$$

with a frequency ν = 0.35 fs^{-1} (photon energy 1.44 eV) and a temporal length τ (the temporal FWHM of the intensity profile is $\tau/\sqrt{2}$). Pulse lengths τ = 10, 25, 50, and 100 fs were used to investigate the pulse length dependence of the electron and nuclear dynamics. The electric field maximum F_M is related to the peak of the effective (i.e., cycle-averaged) intensity I_M (at t = 0) by

$$F_M = \left(\frac{2I_M}{c\varepsilon_0}\right)^{1/2} \quad (3)$$

with the velocity of light c and the dielectric constant of the vacuum ε_0. The laser magnetic field is

$$B_1(t) = B_M\exp[-4\ln(2)(t/\tau)^2]\cos(2\pi\nu t) \quad (4)$$

$$B_M = \left(\frac{2\mu_0 I_M}{c}\right)^{1/2} \quad (5)$$

with the permeability of the vacuum μ_0. In this paper we shall use Å, fs, and eV for length, time, and energy, respectively, while charges and masses are expressed as dimensionless integer multiples of the elementary charge and of the electron rest mass m_e, respectively. In this unit system ε_0 = 5.5270·10^{-3} eV^{-1}Å^{-1}, μ_0 = 2.0131·10^{-5} eVÅ^{-1} fs^2, and c = 2.9979·10^3 Å fs^{-1}. The relations of the electric and magnetic peak intensities F_M and B_M, eqs 3 and 5, with the macroscopic laser intensity I_M (given in W cm^{-2}) are:

$$F_M = 2.7448 \cdot 10^{-7} I_M^{1/2} \quad (6)$$

$$B_M = 9.1555 \cdot 10^{-11} I_M^{1/2} \quad (7)$$

where F_M is given in eVÅ^{-1} and B_M is given in eVÅ^{-2} fs units. The laser propagation direction is taken along the z axis, with the electric field directed along the x axis and the magnetic field along the y axis. The pulse, eqs 1–7, is defined for t > –∞ and the peak of the pulse is attained at t = 0. An initially truncated pulse was used in the simulations, with the initial laser electric field being $F_1 = F_{th}$ at the finite (negative) time t_s, where F_{th} is the threshold field for the first (single electron) ionization of the Xe atom by the BSI mechanism. This choice of t_s will be presented below, and neglects electron tunneling, which is justified for $I_M \geq 10^{15}$ W cm^{-2}.[16,21] Although the gradual (Gaussian) decay of the laser envelope function was applied in the simulations, for further analysis of the trajectories it is convenient to characterize the temporal end of the laser pulse at t = $-t_s$, where $t_s \ll t_L$, with t = t_L being the temporal end ("long time") of the trajectories and t_L–t_s their temporal lengths.

We shall now outline the methodology of the BSI model for cluster inner ionization. The critical electric field strength F for the $Xe^{q+} \rightarrow Xe^{(q+1)+}$+e ionization is[16,21]

$$F = \frac{P_{q+1}^2}{4\overline{B}(q + 1)q_e^2} \quad (8)$$

with the ionization potential P_{q+1}, the electron charge $q_e = -1$, q for the charge of the initial ion or atom (prior to ionization), and $\overline{B} = 1/(4\pi\varepsilon_0)$ = 14.40 eVÅ. The position vector of the barrier location relative to the parent ion is

$$\mathbf{r}_b = \left(\frac{\overline{B}(q + 1)}{F^3}\right)^{1/2} \mathbf{F} \quad (9)$$

with F = |$\mathbf{F}$|. The initial threshold field F_{th} = F for the first ionization is obtained from eq 8 with q = 0 and P_1 = 12.1 eV for Xe.[36] For the initial molecular dynamics setup, $\mathbf{F}$ is merely taken as the external laser field.

Combining eqs 2, 3, and 8, one obtains the initial time t_s for a Gaussian field envelope

$$t_s =$$
$$-\tau\left\{\frac{1}{4\ln(2)}\ln\left[\frac{8\overline{B}(q+1)q_e^2}{P_1^2}\left(6.2415\cdot10^{-13}\frac{2\pi\overline{B}}{c}I_M\right)^{1/2}\right]\right\}^{1/2} \quad (10)$$

with $q = 0$, $P_1 = 12.1$ eV, and I_M being given in W cm^{-2}. The values of $|t_s/\tau|$, obtained from eq 10 for Xe$_n$, are 0.664, 0.926, 1.128, 1.299, 1.450, and 1.587 for $I_M = 10^{15}$, 10^{16}, 10^{17}, 10^{18}, 10^{19}, and 10^{20} W cm^{-2}, respectively. The initial molecular dynamics setup consists of singly charged atoms and of the corresponding stripped electrons, which are placed at the BSI barriers of their Xe$^+$ parent ions. Subsequent BSI processes were described by eqs 8 and 9 with the appropriate P_{q+1} and q values.[21,36] The composite electric field is the superposition of the external laser field and the inner electrostatic field generated by all ions and nanoplasma electrons. In the calculation of the inner field, a cutoff radius r_{BSI} was introduced for the electron–ion distance. The contributions to the inner field of electrons at distances $r < r_{BSI}$ from the center of an ion were excluded in order to avoid the inclusion of spurious field ionization induced by closely located electrons. The simulations for Xe$_{13}$ clusters at $I_M = 10^{15}$ W cm^{-2} (where the effects of electron–atom interactions are the largest) showed a weak dependence (<10%) of the average ionization level on r_{BSI} in the range $r_{BSI} = 1.5$ Å–3.4 Å. We have chosen $r_{BSI} = 2.6$ Å (where the electric field generated by an electron at this distance is 2.2 eVÅ^{-1}, which is smaller than the field of 3.90 eVÅ^{-1} required for the field ionization of Xe → Xe$^+$ + e). The contribution to inner ionization of a close proximity electron–ion interaction at $r_{BSI} < 2.6$ Å is incorporated in the EII mechanism (Section 3 below). Each electron produced by the BSI was initially placed with zero kinetic energy at the BSI barrier of its Xe^{q+} parent ion. In view of the efficient acceleration of the BSI-produced electrons by the composite electric field, we expect that the electron dynamics is insensitive to the initial velocity.

The electron–ion interactions were represented by a Coulomb attraction potential with a smoothing term[27]

$$U_{e-i} = \overline{B}qq_e(r^6 + r_0^6)^{-1/6} \quad (11)$$

with the smoothing parameter $r_0 = 1.0$ Å. By the smoothing term the steep attractive part for short ion–electron distances is avoided and therefore the energy conservation of the molecular dynamics simulations is improved. For the same reason, the short-range ion–electron repulsion term is not included. For the electron–electron potential a smoothing quadratic term was taken as[21,27]

$$U_{e-e} = \overline{B}q_e^2\left(r^2 + \overline{r}_0^2\right)^{-1/2} \quad (12)$$

with $\overline{r}_0 = 0.2$ Å. The ion–ion potential is

$$U_{i-i} = \overline{B}q_1q_2/r_{12} \quad (13)$$

where q_1 and q_2 stand for the q_1-fold and q_2-fold ionized atoms. Unlike for the ion–electron and for the electron–electron potential, a smoothing term is not included in the ion–ion potential, as the dynamics does not involve close ion–ion encounters.

The Cartesian coordinates of the Lorentz force **F** on a particle moving in the laser magnetic field, which acts in the y direction, are

$$F_x = -qv_zB_y$$
$$F_y = 0$$
$$F_z = qv_xB_y \quad (14)$$

As the Lorentz force was considered both for ions and electrons, q in eq 14 stands for either the (integer) ion charge or for the electron charge, $q_e = -1$.

A five-value Gear predictor–corrector algorithm[37] was used to integrate the equations of motion. High-energy electron dynamics for laser intensities of ≥10^{18} W cm^{-2}, e.g., for a Xe$_{2171}$ cluster near the peak of the 10^{18} W cm^{-2} laser pulse, exhibited an average kinetic energy of 72 keV, corresponding to average velocity of $v = 1450$ Å fs^{-1} (with v/c = 0.48) and a maximum electron velocity of v/c = 0.69. Thus the high-energy electron dynamics requires a relativistic treatment, while for the much slower nuclei the Newtonian dynamics suffices. Since the predictor step is merely a polynomial expansion of the positions and its time derivatives, it remains unaffected and the relativistic corrections enter only through the corrector step by modifying the expressions of the Cartesian acceleration components a_x, a_y, a_z:

$$a_x = \beta^{3/2}m_e^{-1}F_{Tx} + \beta^{1/2}m_e^{-1}F_{Nx}$$
$$a_y = \beta^{3/2}m_e^{-1}F_{Ty} + \beta^{1/2}m_e^{-1}F_{Ny} \quad (15)$$
$$a_z = \beta^{3/2}m_e^{-1}F_{Tz} + \beta^{1/2}m_e^{-1}F_{Nz}$$

with $\beta = 1 - v^2/c^2$. F_{Tx}, F_{Ty}, F_{Tz}, and F_{Nx}, F_{Ny}, F_{Nz} are the Cartesian coordinates, respectively, of the tangential and of the normal force components, i.e., of the force components in the flight direction of the corresponding electron and perpendicular to it. A time step of 1 attosecond was used to integrate the equations of motion of the electrons for intensities of 10^{15}–10^{19} W cm^{-2} and 0.5 attoseconds for $I_M = 10^{20}$ W cm^{-2}. The integration time step for the equations of motion of the nuclei was 20 attoseconds. At every electronic time step, the critical BSI electric field strength, eq 8, was checked for every atom. When the critical field strength was exceeded, an electron was placed at the BSI barrier, eq 9. Multiple

ionization is then realized in a sequential way. The criterion for outer ionization, which was checked every 20 attoseconds, was that an electron was farther away from the center of mass of the cluster than six times the instantaneous distance of the outermost atom of the expanding cluster. An electron that met the outer ionization criterion was excluded from the further MD simulation.

In view of the strong ion–ion and electron–ion interactions, the detailed initial structures of the neutral Xe_n clusters and of the singly charged $(Xe^+)_n$ clusters (that correspond to the initial conditions of our simulations) are of minor importance. In our simulations we have used initial closed spherical fcc structures (at $t = -t_s$), with a nearest-neighbor distance of 4.33Å, corresponding to $n = 13, 55, 135, 249, 459, 1061$, and 2171. We note in passing that the number of atoms of closed spherical fcc initial structures is distinct from those of icosahedral closed shell structures of rare gas clusters. However, these differences are insignificant for the simulations of ultraintense laser–elemental cluster interactions.

The simulations were carried out using a Silicon Graphics Origin 3200, Itanium-2, 1.4 GHz single processor. The longest computation times were used for the largest cluster at the lowest intensity. For Xe_{2171} clusters at intensity $I_M = 10^{15}$ W cm^{-2}, the computation time was 15.7 days for $\tau = 25$ fs and a trajectory length of 110 fs, while the computation time was 45.2 days for $\tau = 100$ fs and a trajectory length of 250 fs.

3. ELECTRON IMPACT IONIZATION

In our simulations we have included single EII processes

$$Xe^{q+} + e \rightarrow Xe^{(q+1)+} + 2e \qquad (16)$$
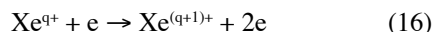
for the formation of the nanoplasma, while electron impact multi-ionization processes

$$Xe^{q+} + e \rightarrow Xe^{(q+m)+} + (m+1)e; \ m>1 \qquad (17)$$
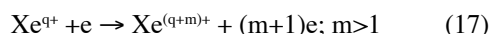
have been disregarded. Experimental data for electron impact cross sections $\sigma_q(E)$, as functions of the impact energy E, are available up to $q = 10$.[38] The peak values for the EII cross sections[38] decrease by a numerical factor of 40 from $q = 1$ to $q = 10$, providing a plausibility argument for restricting the q region for EII. In a recent paper[27] we have fitted the experimental data to a simplified version of the Lotz formula[39]

$$\sigma_q(E) = a_q \frac{\ln(E/P_{q+1})}{EP_{q+1}} \left\{ 1 - b_q \exp\left[-c_q\left(E/P_{q+1} \right) \right] \right\} \qquad (18)$$

with the atomic ionization energy P_{q+1} (ref 36) and the adjustable parameters a_q, b_q, and c_q, which were obtained by fitting eq 18 to the experimental cross sections. The

Table 1. Parameters for the fit of the experimental data[38] for the cross sections for electron impact ionization $Xe^{q+} \rightarrow Xe^{(q+1)+} + 2e$, according to the Lotz equation, eq 18

q	$a_q/10^{-13}$ cm^2 (eV)^2	b_q	c_q	P_{q+1}/eV
1	2.62	−0.50	0.70	21.21
2	2.36	−1.40	0.35	32.1
3	3.22	−3.10	1.10	46.7
4	2.87	−3.20	2.20	59.7
5	8.96	0.08	0.05	71.8
6	9.43	−0.90	2.20	92.1
7	7.43	0	0	105.9
8	6.76	−0.40	0.35	171
9	7.21	−0.27	0.16	202
10	6.67	−0.42	0.18	233

ionization energies P_{q+1} and the parameters a_q, b_q, c_q are listed in Table 1.

EII takes place if the kinetic energy of the impinging electron exceeds the ionization energy and if its impact parameter d is smaller than the effective radius $r = (\pi\sigma)^{1/2}$ of the particular ionization level, where σ is the corresponding cross section. The implementation of EII in clusters requires the basic approximation that the cross sections $\sigma_q(E)$ are unaffected by the ion–electron, electron–electron, and ion–ion interactions within the cluster, and that the corresponding single atom cross sections, eq 18, will be used. Some further modifications are required for the cluster impact ionization events as compared to those of isolated atoms. First, atomic ionization energies are defined for an electron being moved to an infinite distance from the parent ion. But since the ions and the electrons are initially located inside the cluster, the ejected electron must be placed at some finite distance from the parent ion, which requires corrections for the energetics. Second, an impact parameter refers to an infinite distance of the impinging electron before the impact. However, in the cluster the electron comes from a finite distance and is deflected by other cluster particles. Third, the velocity of the impinging electron prior to and after impact ionization, as well as of the ejected electron, is affected by the cluster environment.

In order to keep the computational effort moderately small, the treatment of EII rests on a simple sequential one-electron scheme. Only stepwise sequential ionizations, eq 16, are considered. EII is considered if a particular electron approaches an ion at a distance closer than 2 Å, which is considerably smaller than the interatomic Xe–Xe distance of 4.3 Å at the beginning of the simulation. The possibility of EII is checked for all electrons at each electronic time step (0.5–1 attosecond). It is imperative to use this shorter time interval of 0.5–1 attosecond since an electron can pass several tenths of an angstrom

per attosecond. For a separated electron–ion pair the impact parameter is given by[40]

$$d = L m_e^{-1} c^{-1} \left[1 - \left(\frac{m_e c^2}{E_{kin,\infty} + m_e c^2} \right)^2 \right]^{-1/2} \quad (19)$$

where L is the absolute value of the angular momentum of the electron within the electron–ion pair (with the ion at rest), m_e is the electron mass, and $E_{kin,\infty}$ is the kinetic energy of the electron at infinity. Equation 19 is based on the fact that the electron velocity v_∞ at an infinite distance is by definition perpendicular to the impact parameter d, so that the vector product $\mathbf{L} = m\mathbf{r} \times \mathbf{v}$ of the position $\mathbf{r}$ and velocity $\mathbf{v}$ may be replaced by the corresponding scalar quantities d and v_∞, where v_∞ can be calculated from the kinetic energy $E_{kin,\infty}$ according to the general relativistic relation between velocity and kinetic energy

$$v = c \left[1 - \left(\frac{m_e c^2}{E_{kin} + m_e c^2} \right)^2 \right]^{-1/2} \quad (20)$$

$E_{kin,\infty}$ can be calculated from the instantaneous kinetic energy $E_{kin,r}$ at the electron–ion distance r

$$E_{kin,\infty} = E_{kin,r} + \frac{\overline{B} q q_e}{\left(r^6 + r_0^6 \right)^{1/6}} \quad (21)$$

The correction term in eq 21 accounts for the conversion of kinetic into potential energy. Equations 19 and 21 are exact for the isolated ion–electron subsystem. The approximate nature of this treatment originates from neglecting all other cluster particles. L, which is constant only for the isolated ion–electron pair, was evaluated when the electron–ion distance falls below the 2 Å limit, i.e., at the instant when the possibility of an EII has to be checked for.

The impinging and the ejected electrons in the EII were treated by keeping the location of the impinging electron unchanged. The ejected electron is placed at the same distance from the ion, but in an angular distance of 60° from the impinging electron. The angle of 60° was chosen so that the two electrons and the parent ion form an equilateral triangle. After impact ionization the kinetic energy $E_{kin,final}$ available for both electrons is given (in eV) by

$$E_{kin,final} = -\overline{B} \frac{q_e(q_A + 1)}{\left(r_{Ak}^6 + r_0^6 \right)^{1/6}} - P_{q+1} - \overline{B} \sum_{a \neq A} \left(\frac{q_e q_a}{\left(r_{ak}^6 + r_0^6 \right)^{1/6}} \right)$$
$$+ \overline{B} \sum_{a \neq A} \left(\frac{q_e q_a}{\left(r_{aA}^6 + r_0^6 \right)^{1/6}} \right) - \overline{B} \sum_i \left(\frac{q_e^2}{\left(r_{ik}^2 + \overline{r}_0^2 \right)^{1/2}} \right)$$
$$- \overline{B} \sum \left(\frac{q_e^2}{\left(r_{iA}^2 + \overline{r}_0^2 \right)^{1/2}} \right) + m_e c^2 \left(\frac{1}{\left(1 - v_l^2/c^2 \right)^{1/2}} - 1 \right) \quad (22)$$

where A denotes the Xe^{q+} ion where the impact takes place, k is the ejected electron, and l is the impact electron. q_A is the charge of ion A before the impact. The first term in eq 22 represents the potential energy of the ejected electron in the field of ion A after the impact ionization. The third and the fourth terms in eq 22 are the potential energy difference of the ejected electron k in the field of all other ions a, after and before the impact ionization, respectively. The fifth and the sixth terms are the potential energy difference of electron k in the field of all other electrons i including the impinging electron l. It is assumed that before the impact ionization electron k is located in the center of ion A, so that the distance of electron k to all other ions and electrons is r_{aA} and r_{iA}, respectively. The last term of eq 22 is the relativistic kinetic energy of the impinging electron before the impact ionization.

The kinetic energy $E_{kin,final}$ after the impact is equally allocated to the impinging and to the ejected electrons; the absolute velocities of the two electrons after impact are given by eq 20, with $E_{kin} = E_{kin,final}/2$. In our simulations the impinging and the ejected electrons were given by the velocity direction of the impinging electron before impact with a superimposed Gaussian-weighted random deviation. That is to say, the most likely direction of the two electrons after impact is the original flight direction before impact. While the total energy is conserved in this way, the linear and angular momentums are not, but this is a small error in view of the large cluster mass.

The random contribution to the electron flight directions is an alternative to running different trajectories with different initial conditions. Due to the enormous computational effort, most of the results presented in this work are single-trajectory results. In the test cases, when several trajectories were run for the same cluster size and laser intensity but with a different seed of the random number generator, the largest difference of the number of impact ionizations was <10% and in most cases much smaller. After EII, the impinging and the ejected electrons are excluded by the simulation algorithm from further impact ionizations at the same parent ion, as long as they are inside the distance of approach of 2 Å for impact ionization. In this way, multiple impact ionizations are ruled out. In our previous simulations,[21,27] the algorithm for the avoidance of multiple ionizations was unsatisfactory, precluding further impact ionizations at an ion, even if an EII attempt was unsuccessful. While the impact ionization yields reported in our recent paper[27] are larger by roughly a numerical factor of ~2, as compared with the results of an older simulation[21] in which the electron impact cross sections were treated in a much more approximate way, these impact ionization yields[27] are still smaller by a numerical

factor of ~2 as compared with the results reported in our present work because of the unsatisfactory avoidance of multiple impact ionizations in our previous work.[27]

We note in passing that the effects of electron–ion recollision including (e, 2e) processes[41,42] are intrinsically included in our treatment of impact ionization. These effects of electron–ion recollision are of considerable importance at lower intensities ($I_M < 10^{15}$ W cm^{-2}), where electron tunneling effects in the BSI[1,4,21] also have to be incorporated.

4. VALIDITY CONDITIONS FOR THE TREATMENT OF ELECTRON DYNAMICS

The validity conditions for the applicability of classical MD simulations to the high-energy nanoplasma electrons rest on the conditions for the localization of the wave packet[43] and for the distinguishability of identical particles,[44] which will be addressed for the Xe$_n$ cluster.

(A) The wave packet localization condition[43] implies that the de Broglie wavelength $\lambda_{DB} = h(2m_e\varepsilon)^{-1/2}$, where ε is the nanoplasma single electron kinetic energy, is considerably shorter than the interelectron separation, $r_{ee} = 2R_0/(nq_{av})^{1/3} = 2r_0/q_{av}^{1/3}$, where R_0 is the cluster radius, $r_0 = R_0/n^{1/3} = 2.16$ Å is the constituent radius, n the number of constituents, and $q_{av} = n_{ii}^L$ the average ionization level of each Xe (where n_{ii}^L is the long-time inner ionization level per constituent atom introduced in Section 5). The wave packet localization condition is $\lambda_{DB} < r_{ee}$. In Table 2 we present our simulation results for q_{av} (Section 3) and for the average kinetic energy $\in$ at $t = 0$, which corresponds to the laser pulse peak (with a marked increase with increasing I_M). From the results of Table 2 we infer that the wave packet localization condition is weakly satisfied (i.e., $\lambda_{DB} < r_{ee}$) in the intensity range $I_M = 10^{15}$–10^{16} W cm^{-2} and is well satisfied (i.e., $\lambda_{DB} << r_{ee}$) at $I_M \geq 10^{18}$ W cm^{-2}.

(B) The distinguishability condition for identical (fermion) particles implies that the neglect of quantum permutation symmetry constraints is valid provided

Table 2. Validity condition for the applicability of molecular dynamics simulations to the nanoplasma electrons in Xe$_n$ clusters

I_M W cm^{-2}	q_{av} [a]	$\in$ eV [b]	λ_{DB} Å	r_{ee} Å	λ_{DB}/r_{ee}
10^{15}	5	53	1.5	2.52	0.59
10^{16}	8	147	1.0	2.16	0.48
10^{17}	15	933	0.41	1.75	0.23
10^{18}	23	$72 \cdot 10^3$	0.046	1.52	0.030
10^{19}	26	$100 \cdot 10^3$	0.039	1.45	0.027
10^{20}	36	$>10^6$	0.012	1.31	0.0092

[a] Average ionic charge for {Xe^{q+}} ions from a Xe$_{2171}$ cluster.
[b] Average kinetic energy of nanoplasma electrons (per electron) in Xe$_{2171}$ at the laser peak (t = 0).
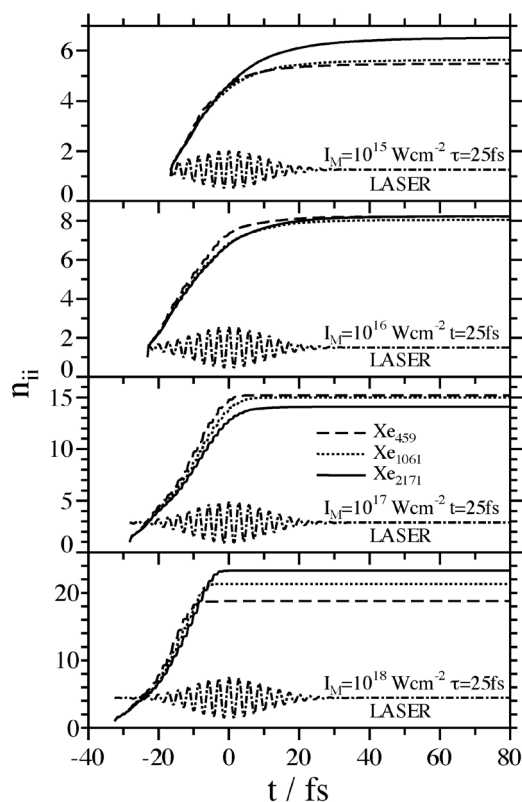
Fig. 1. The time dependence of the inner ionization levels n_{ii} per constituent atom for Xe$_n$ clusters (n = 459, 1061, 2171 as marked on the panels) for the intensities $I_M = 10^{15}$ W cm^{-2}, 10^{16} W cm^{-2}, 10^{17} W cm^{-2}, and 10^{18} W cm^{-2}. The laser pulse width is $\tau = 25$ fs. The electric fields of the Gaussian laser pulses (– · – · –), expressed in arbitrary units for $t \geq t_s$, are represented on each panel, marked LASER.

that[44] $f = \exp[-(r_{ee}/\lambda_{DB})^2] << 1$. From the data of Table 2 it appears that the distinguishability condition is satisfied over the entire intensity domain that is of interest to us.

5. INNER IONIZATION LEVELS

Simulation results were attained for inner/outer ionization levels and for the population of the nanoplasma in Xe$_n$ clusters. In Fig. 1 we present the time dependence of the inner ionization levels $n_{ii}(t)$ per constituent atom ($I_M = 10^{15}$, 10^{16}, 10^{17}, 10^{18} W cm^{-2}, $\tau = 25$ fs, n = 459, 1061, 2171). The initial cluster charge was taken as $n_{ii}(t_s) = 1$, where t_s is given by eq 10. $n_{ii}(t)$ reveals a gradual increase towards saturation or near-saturation at longer times $-t_s < t \leq t_L$, where $t_L = 92$ fs is the temporal end of the trajectory (Section 2). The "long time" inner ionization levels correspond to the final (average) charges of the {Xe^{q+}} ions, which are amenable to experimental observation.[3,10–15] Consecutively with and parallel to inner ionization, outer ionization occurs, being characterized by the time-dependent outer ionization levels $n_{oi}(t)$
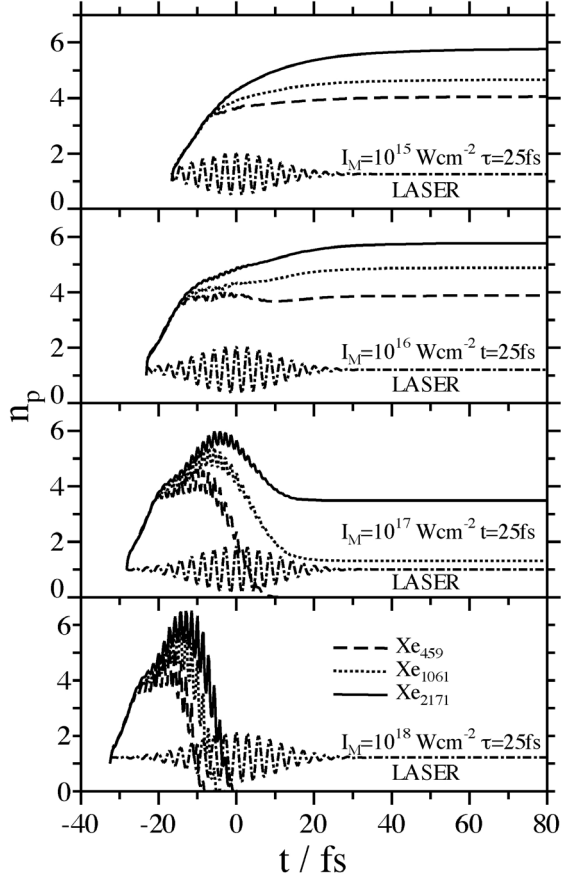
Fig. 2. The time dependence of the nanoplasma population n_p (per constituent atom) for Xe_n clusters (n = 459, 1061, 2171 as marked on the panels) for the intensities $I_M = 10^{15}$ W cm^{-2}, 10^{16} W cm^{-2}, 10^{17} W cm^{-2}, and 10^{18} W cm^{-2}. The laser pulse width is $\tau = 25$ fs. The electric fields of the Gaussian laser pulses ($-\cdot-\cdot-$), expressed in arbitrary units for $t \geq t_s$, are represented on each panel, marked LASER.

Fig. 3. Cluster size and laser intensity dependence of the long-time inner ionization levels (expressed by the average charge of the $\{Xe^{q+}\}$ ions) of the Xe_n clusters (n = 55–2171) over the intensity range $I_M = 10^{15}–10^{20}$ W cm^{-2} (marked on the curves) with the laser pulse widths of $\tau = 10$ fs, 25 fs, 50 fs, and 100 fs. The horizontal arrows (marked atomic limit) represent the single-atom ionization level calculated from the BSI model.

per constituent atom. The number of the electrons in the nanoplasma is $n_p(t) = n_{ii}(t) - n_{oi}(t)$ per constituent atom. The intensity and cluster size dependence of $n_p(t)$ and of the long-time population $n_P^L = n_p(t_L)$ provide information on the production and depletion of the nanoplasma (Fig. 2). In the laser intensity range of $I_M = 10^{15}–10^{16}$ W cm^{-2}, $n_p(t)$ saturates at long times, where n_P^L increases with increasing the cluster size (Fig. 2). On the other hand, at $I_M = 10^{18}$ W cm^{-2}, the nanoplasma is completely depleted before the laser reaches its peak (Fig. 2), with the efficiency of the complete nanoplasma depletion increasing at lower cluster sizes. At the intensity $I_M = 10^{17}$ W cm^{-2}, $n_p(t)$ exhibits an intermediate-type behavior, revealing a long-time saturation for larger clusters and complete depletion for smaller clusters (Fig. 2). This pattern manifests the distinction between the persistent nanoplasma at lower intensities and large cluster sizes
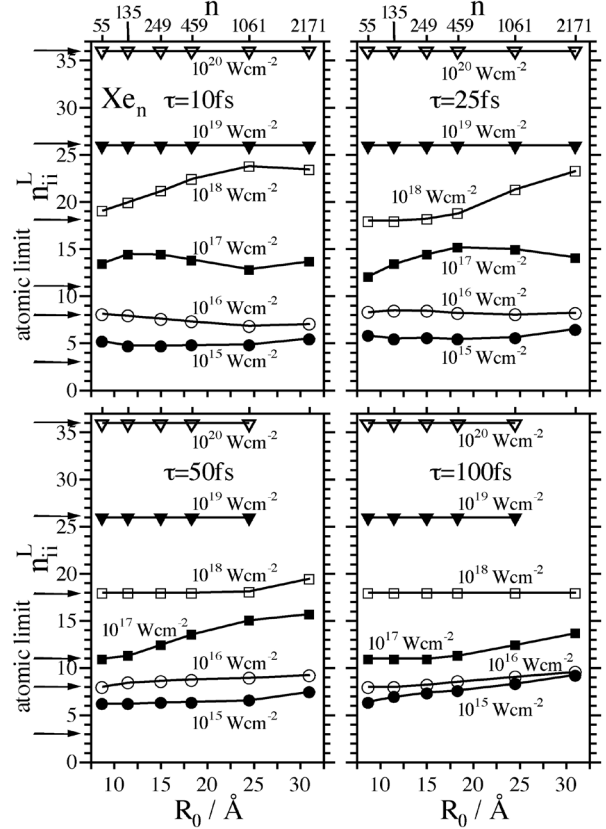
and the transient nanoplasma at higher intensities and smaller cluster sizes.

The cluster inner ionization levels were calculated from the parallel–sequential contributions of BSI and EII. The BSI contribution was calculated from eq 8 and the procedure in Section 2, with the time-dependent electric field

$$\mathbf{F}(t) = \mathbf{F}_l(t) + \mathbf{F}_I(t) \qquad (23)$$

consisting of the superposition of the laser field $\mathbf{F}_l(t)$ and the inner field $\mathbf{F}_I(t) = \mathbf{F}^{(+)}(t) - \mathbf{F}^{(-)}(t)$, which is generated by the electrostatic field exerted on each ion by all the cluster ions ($\mathbf{F}^{(+)}(t)$) and by the nanoplasma electrons ($\mathbf{F}^{(-)}(t)$). The (time-dependent) inner field is enhanced by the ignition effect,[16,21] due to the contribution $\mathbf{F}^{(+)}$ of the positive ions, and is reduced by the screening effect,[16,21] due to the contribution $\mathbf{F}^{(-)}(t)$ of the nanoplasma electrons (Section 2). In Fig. 3 we portray the cluster size (n = 55–2171), laser intensity ($I_M = 10^{15}–10^{20}$ W cm^{-2}),

and pulse length ($\tau = 10$–100 fs) dependence of the long-time outer ionization levels n_{ii}^L of Xe$_n$ clusters. For comparison, the single-atom limits are marked as arrows at the ordinate for all the laser intensities considered herein. n_{ii}^L is determined by the following contributions:

(1) The laser intensity. The ionization levels are determined by the strength of the external laser field, as manifested by the general result that the n_{ii}^L values of the different laser intensities (presented in Fig. 3) are well separated (except from some cases in the lower intensity range 10^{15}–10^{16} W cm^{-2}). For any cluster size and for all values of τ, n_{ii}^L increases with increasing I_M, essentially manifesting the contribution of the laser field to the BSI. In the highest intensity domain, $I_M = 10^{19}$–10^{20} W cm^{-2}, n_{ii}^L is completely independent of τ and n, being equal to the single atom ionization level, and manifesting the dominating contributions of the laser field to the BSI at these highest intensities.

(2) The ignition effect. The ignition effect is manifested by the increase of n_{ii}^L with increasing the cluster size due to the enhancement of the inner electric field by the cluster ions.[16,21] Typical examples, where the ignition effect increases n_{ii}^L beyond the single-atom value and leads to an increase of n_{ii}^L with increasing the cluster size, are given at $\tau = 25$ fs, $I_M = 10^{18}$ W cm^{-2} and at $\tau = 50$ fs, $I_M = 10^{17}$ W cm^{-2}. A dramatic example is provided by the large difference of 3 charges between the n_{ii}^L value of Xe$_{55}$ and the corresponding single-atom value at $I_M = 10^{15}$ W cm^{-2} for all pulse lengths. The ignition effect tends to decrease with increasing τ, because for longer pulses the peak of the laser electric field is reached at a later time, when CE has already set in, so that the maximum of the external field does not coincide anymore with the maximum of the inner field. An example for a diminished ignition effect as a consequence of the increased pulse length is given by the case of $I_M = 10^{18}$ W cm^{-2}, $\tau = 50$ and 100 fs, as compared to the n_{ii}^L values at $\tau = 25$ fs.

(3) The screening effect. Screening is manifested by the decrease of n_{ii}^L with increasing the cluster size, since the nanoplasma electrons are increasingly persistent with increasing the cluster size.[16,21] As outer ionization increases with increasing the pulse length, screening is reduced with increasing τ. The case of $I_M = 10^{16}$ W cm^{-2}, $\tau = 10$ fs constitutes the only example where the screening effect reduces the n_{ii}^L values below the single-atom value. As screening and ignition effect both increase with increasing n, screening is mostly compensated by the ignition

effect. For example, at $\tau = 10$ fs, $I_M = 10^{18}$ W cm^{-2} and at $\tau = 25$ fs, $I_M = 10^{17}$ W cm^{-2}, the ignition effect enhances n_{ii}^L above the single-atom and the screening effect merely causes a slight decrease of n_{ii}^L for large clusters after passing a maximum.

(4) Electron impact ionization. The EII contribution increases with increasing the cluster size and with increasing the laser pulse length. The relative EII yield, n_{imp}^L/n_{ii}^L (n_{imp}^L being the number of electrons per constituent atom generated by EII), increases with increasing the cluster size and with decreasing the laser intensity.[27,30] For Xe$_{2171}$, $I_M = 10^{15}$ W cm^{-2}, $\tau = 100$ fs, EII is the dominating ionization channel.[30] In Fig. 3 the importance of EII is particularly manifested by the breakdown of the predominance of the effect of the external laser field on n_{ii}^L (cf. point (1)), as the n_{ii}^L values for large clusters at $I_M = 10^{15}$ W cm^{-2}, $\tau = 100$ fs almost reach the corresponding values at $I_M = 10^{16}$ W cm^{-2}, $\tau = 100$ fs and even exceed the 10^{16} W cm^{-2} results for $\tau = 10$ fs and 25 fs.

The interplay between ignition effect, screening effect, and EII contributions is complex. Information about the net effect of EII was obtained by additional simulations, in which the EII channel was switched off,[30] simplifying the analysis of the three contributions. An interesting example for the interplay and mutual cancellation of ignition effect, screening effect, and EII contributions is given by the cluster size dependence at $\tau = 10$ fs, $I_M = 10^{17}$ W cm^{-2}. The ignition effect increases the n_{ii}^L values above the single-atom limit over the entire cluster size range and is responsible for the slight increase for small clusters up to Xe$_{249}$. For Xe$_{459}$ and Xe$_{1061}$ the screening effect then causes a decrease of the n_{ii}^L values, while for Xe$_{2171}$ the n_{ii}^L value increases again due to EII.

6. ABSORPTION OF THE LASER ENERGY BY THE CLUSTERS

An implicit assumption inherent in the present work is that the laser intensity I(t) is assumed to be uniform inside the cluster. This assumption is valid provided that the light wavelength λ is much larger than the cluster size, and that the laser light is not noticeably attenuated by absorption while propagating through the cluster. For the laser frequency $\nu = 0.35$ fs^{-1} used in the present work the wavelength is $\lambda = 8750$ Å, being considerably larger than the maximal cluster diameter $2R_0 = 62$ Å (for Xe$_{2171}$) considered herein. The light attenuation was analyzed by the comparison between the energy absorbed by the cluster and the laser energy flow through the cluster. Neglecting the cluster expansion due to CE, the

energy flow through the cluster is $E_f^{CLUSTER} = \pi R_0^2 \int_{-\infty}^{\infty} I(t)dt$, which for a Xe_{2171} cluster ($R_0 = 30.4$ Å) assumes the value $E_f^{CLUSTER} = 1.77 \cdot 10^{-8} I_M$ (with $E_f^{CLUSTER}$ being given in eV and I_M in W cm^{-2}). The energy E_{abs} absorbed by the cluster (per Xe atom) is given by the multielectron ionization energy $\sum_{q=1}^{q_{av}} P_q$, together with the final total energy of all the particles, i.e., the electrons (with the average electron kinetic energy $\in$ for q_{av} electrons per ion, Table 2) and the ions (with the average kinetic energy $E_{av} = 1$ keV–1 MeV per ion for CE[1,4,23,24]). Accordingly

$$E_{abs} = \sum_{q=1}^{q_{av}} P_q + q_{av} \in + E_{av} \qquad (24)$$

For Xe_n clusters at $I_M = 10^{15}$–10^{16} W cm^{-2}, the three terms in eq 24 contribute to E_{abs} at $I_M = 10^{17}$–10^{18} W cm^{-2}, the contribution originates from the electron and ion kinetic energies, while at $I_M = 10^{19}$–10^{20} W cm^{-2} the dominating contribution arises from the electron kinetic energy. Over the entire intensity domain of $I_M = 10^{15}$–10^{20} W cm^{-2} we find the ratio of the energy nE_{abs} absorbed in the cluster and the energy flow $E_f^{CLUSTER}$ to vary irregularly in the range $nE_{abs}/E_f^{CLUSTER} = 0.04$–$0.23$. The moderately small contribution of the laser absorption for the largest Xe_{2171} clusters used herein justifies the neglect of the attenuation of light intensity inside the clusters. With increasing the cluster size, we expect that the ratio of the energies obeys a scaling law $nE_{abs}/E_f \propto R_0^{\eta}$ where $\eta \leq 3$,[31,45] with this ratio increasing with increasing the cluster size. When $nE_{abs}/E_f^{CLUSTER} \gtrsim 1$, our treatment has to be extended to account for the attenuation of the ultraintense laser absorption by a single cluster.[45]

7. DISCUSSION

While the use of classical MD simulations for the dynamics of nuclei is standard, the application of this approach for the dynamics of high-energy electrons required the specification of proper validity conditions (Section 3). Two comments are in order regarding the application of MD simulations for the nanoplasma electron dynamics in Xe_n clusters. First, both the length scales of the de Broglie electron wavelength λ_{DB} and of the (mean) interelectron distance r_{ee} increase with decreasing I_M. For the nanoplasma in highly ionized Xe_n clusters (with q electrons per ion) this situation is qualitatively different from $(H_2)_n$ or $(D_2)_n$ clusters (with one nanoplasma electron per atom). In the latter case, when decreasing I_M, λ_{DB} increases, while $r_{ee} = r_0$ remains nearly constant. Second, our use of MD for electron dynamics at $I_M = 10^{15}$ W cm^{-2} touches on the upper limit for the ratio λ_{DB}/r_{ee}, which is physically acceptable to justify the wave packet localization condition. Concurrently, the distinguishability of identical particles is

well satisfied for $I_M \geq 10^{15}$ W cm^{-2}. Recent simulations of electron dynamics by Vrakking and coworkers[46] on optimal control of Xe_n clusters in laser fields at $I_M = (1.2–3.5)10^{14}$ W cm^{-2}, descend below the validity limit for the applicability of classical MD simulations. Future simulations, based on quantum path integral MD (with the neglect of exchange),[44] can be utilized for the dynamics of the nanoplasma electrons. The application of density functional methods[47,48] will also be of interest.

Our MD computational methods are applicable for the description of electron and nuclear dynamics in elemental and molecular clusters containing up to thousands of constituents, e.g., Xe_n ($n \leq 3 \cdot 10^3$)[21,27,29,30] or $(D_2)_n$ ($n \leq 3 \cdot 10^4$)[23]. Driven by ultraintense laser–cluster interactions, the extreme multielectron ionization processes are followed by CE of highly charged ions[1,4,21,24] or bare nuclei.[24,32] The energies of the product ions or nuclei increase with increasing the cluster size, as shown experimentally[10–15] and established theoretically with the advent of scaling laws for CE energetics.[14,17,18,23,24,28] Efficient dd nuclear fusion[11–15] or nucleosynthesis[32] driven by cluster CE requires the use of large clusters[11–14] or even nanodroplets.[15,32] The direct MD simulations of ionization levels and CE of very large clusters, "where each particle counts", require unrealistic computation times. Computational methods for very large finite systems were advanced using a hierarchical tree method[7,49] or a particles-in-cell code.[50,51] We advanced[52] a new scaling procedure, which reduces the effective number of particles in the MD simulations. This scaling method allows for simulations of electron and CE dynamics of very large molecular and elemental clusters (with n = 10^6–10^7).

REFERENCES AND NOTES

(1) Saalmann, U.; Siedschlag, Ch.; Rost, J.M. *J. Phys. B* **2006**, *39*, R39.

(2) Ditmire, T.; Tisch, J.W.G.; Springate, E.; Mason, M.B.; Hay, N.; Smith, R.A.; Marangos, J.; Hutchinson, M.H.R. *Nature* **1997**, *386*, 54.

(3) Ditmire, T. *Phys. Rev. A* **1998**, *57*, R4094.

(4) Krainov, V.P.; Smirnov, M.B. *Phys. Rev.* **2002**, *370*, 237.

(5) Saalmann, U.; Rost, J.M. *Phys. Rev. Lett.* **2002**, *89*, 132401.

(6) Lezius, M.; Blanchet, V.; Ivanov, M.Yu.; Stolow, A. *J. Chem. Phys.* **2002**, *117*, 1575.

(7) Saalmann, U.; Rost, J.-M. *Phys. Rev. Lett.* **2003**, *91*, 223401.

(8) Siedschlag, Ch.; Rost, J.-M. *Phys. Rev. A* **2003**, *67*, 13404.

(9) Siedschlag, Ch.; Rost, J.-M. *Phys. Rev. Lett.* **2004**, *93*, 043402.

(10) Madison, K.W.; Patel, P.K.; Allen, M.; Price, D.; Fitzpatrick, R.; Ditmire, T. *Phys. Rev. A* **2004**, *70*, 053201.

(11) Zweiback, J.; Cowan, T.E.; Smith, R.A.; Hurtlay, J.H.; Howell, R.; Steinke, C.A.; Hays, G.; Wharton, K.B.; Krane, J.K.; Ditmire, T. *Phys. Rev. Lett.* **2000**, *84*, 2634.

(12) Zweiback, J.; Cowan, T.E.; Hartley, J.M.; Howell, R.; Wharton, K.B.; Crane, J.K.; Yanovski, V.P.; Hays, G.; Smith, R.A.; Ditmire, T. *Phys. Plasmas* **2002**, *9*, 3108.

(13) Madison, K.W.; Patel, P.K.; Allen, M.; Price, D.; Fitzpatrick, R.; Ditmire, T. *Phys. Rev. A* **2004**, *70*, 053201.

(14) Grillon, G.; Balcou, Ph.; Chambaret, J.-P.; Hulin, D.; Martino, J.; Moustaizis, S.; Notebaert, L.; Pittman, M.; Pussieux, Th.; Rousse, A.; Rousseau, J.-Ph.; Sebban, S.; Sublemontier, O.; Schmidt, M. *Phys. Rev. Lett.* **2002**, *89*, 065005.

(15) Ter-Avertisyan, S.; Schnürer, M.; Hilscher, D.; Jahnke, U.; Bush, S.; Nicles, P.V.; Sandner, W. *Phys. Plasmas* **2005**, *12*, 012702.

(16) Last, I.; Jortner, J. *Phys. Rev. A* **2000**, *62*, 013201.

(17) Last, I.; Jortner, J. *Phys. Rev. Lett.* **2001**, *87*, 033401.

(18) Last, I.; Jortner, J. *Phys. Rev.* **2001**, *64*, 063201.

(19) Last, I.; Levy, Y.; Jortner, J. *Proc. Natl. Acad. Sci. USA* **2002**, *99*, 9107.

(20) Last, I.; Jortner, J. *Chem. Phys. Chem.* **2002**, *3*, 845.

(21) Last, I.; Jortner, J. *J. Chem. Phys.* **2004**, *120*, 1336.

(22) Last, I.; Jortner, J. *J. Chem. Phys.* **2004**, *120*, 1348.

(23) Last, I.; Jortner, J. *J. Chem. Phys.* **2004**, *121*, 3030.

(24) Last, I.; Jortner, J. *J. Chem. Phys.* **2004**, *121*, 8329.

(25) Last, I.; Jortner, J. *Phys. Rev. A* **2005**, *71*, 063204.

(26) Levy, Y.; Last, I.; Jortner, J. *J. Chem. Phys.* **2005**, *123*, 154301.

(27) Heidenreich, A.; Last, I.; Jortner, J. *Eur. Phys. J. C* **2005**, *35*, 567.

(28) Heidenreich, A.; Last, I.; Jortner, J. *Proc. Natl. Acad. Sci. USA* **2006**, *103*, 10589.

(29) Heidenreich, A.; Last, I.; Jortner, J. *Is. J. Chem. (special issue in honor of R.N. Zare)* **2007**, *47*, in press.

(30) Heidenreich, A.; Last, I.; Jortner, J. *Laser Phys.* **2007**, *17*, 608.

(31) Last, I.; Jortner, J. *Phys. Rev. A* **2006**, *73*, 013202.

(32) Last, I.; Jortner, J. *Phys. Rev. Lett.* **2006**, *97*, 173401.

(33) "Research Highlights", *Nature* **2006**, *444*, 127.

(34) Mijoule, V.; Lewis, L.J.; Meunier, M. *Phys. Rev. A* **2006**, *73*, 033203.

(35) Petrov, G.M.; David, J. *Phys. Plasmas* **2006**, *13*, 003106.

(36) Cowan, R.D. *The Theory of Atomic Structure and Spectra*; University of California Press: Berkeley, CA, 1981.

(37) Gear, C.W. *Numerical Initial Value Problems in Ordinary Differential Equations*; Prentice-Hall: Englewood Cliffs, NJ, 1971.

(38) (a) Achenbach, C.; Mueller, A.; Salzborn, E.; Becker, R. *J. Phys. B.* **1984**, *17*, 1405. (b) Griffin, D.C.; Bottcher, C.; Pindzola, M.S.; Younger, S.M.; Gregory, D.C.; Crandall, D.H. *Phys. Rev. A* **1984**, *29*, 1729. (c) Gregory, D.C.; Crandall, D.H. *Phys. Rev. A* **1983**, *27*, 2338. (d) Bannister, M.E.; Mueller, D.W.; Wang, L.J.; Pindzola, M.S.; Griffin, D.C.; Gregory, D.C *Phys. Rev. A* **1988**, *38*, 38. (e) Hofmann, G.; Neumann, J.; Pracht, U.; Tinschert, K.; Stenke, M.; Voelper, R.; Salzborn, E. *AIP Conference Proceedings*; International Conference of Highly Charged Ions (1992) **1993**, *274*, 485.

(39) Lotz, W. *Z. Phys.* **1968**, *216*, 241.

(40) Landau, L.D.; Lifschitz, E.M. *Mechanics*; Pergamon Press: Oxford, 1960.

(41) Corkum, P.B. *Phys. Rev. Lett.* **1993**, *71*, 1994.

(42) Bhardwaj, V.R.; Corkum, P.B.; Rayner, D.M. *Phys. Rev. Lett.* **2004**, *93*, 043001.

(43) Allen, M.P.; Tildesley, D.J. *Computer Simulations of Liquids*; Clarendon Press: Oxford, 1992.

(44) Feynman, R.P.; Hibbs, A.R. *Quantum Mechanics and Path Integrals*; McGraw-Hill: New York, 1965.

(45) Last, I.; Jortner, J. *Phys. Rev. Lett.* **2006**, *97*, 173401.

(46) Springate, E.; Siedschlag, Ch.; Samith, S.; Muller, H.G.; Vrakking, M.J.J. *Phys. Rev. A* **2005**, *72*, 053202.

(47) Sharkofsky, I.P.; Johnston, T.W.; Bachynski, M.P. *The Particle Kinetics of Plasmas*; Addison Wesley: New York, 1966.

(48) Fennel, T.; Bertsch, G.F.; Meiwes-Broer, K.H. *Eur. Phys. J. D* **2004**, *29*, 367.

(49) Pfalzner, S.; Gibbon, P. *Phys. Rev. E* **1998**, *57*, 4698.

(50) Zheng, J.; Sheng, Zh.-M.; Peng, X.-Y.; Zhang, J. *Phys. Plasmas* **2005**, *12*, 113905.

(51) Jungreuthmayer, Ch.; Geissler, M.; Brabec, Th. *Phys. Rev. Lett.* **2004**, *92*, 133401.

(52) Last, I.; Jortner, J. *Phys. Rev. A* **2007**, *75*, 042507.

(53) Jortner, J.; Levine, D.; Ottolenghi, M.; Stein, G. *J. Phys. Chem.* **1961**, *65*, 1232.